Available online at www.sciencedirect.com
SCIENCE DIRECT®
Acta Materialia 52 (2004) 1283–1295
Acta MATERIALIA
www.actamat-journals.com

Synthesis, structure, and mechanical properties of Ni–Al and Ni–Cr–Al superalloy foams

Heeman Choe *, David C. Dunand

Department of Materials Science and Engineering, Northwestern University, 2220 Campus Drive, Evanston, IL 60208, USA

Received 11 September 2003; received in revised form 15 November 2003; accepted 17 November 2003

Abstract

Reticulated nickel foams were alloyed with 8–9 wt% Al or 14–18 wt% Cr and 5–9 wt% Al in a three-step method consisting of (i) gas-phase deposition of Cr and/or Al onto the struts of a pure Ni foam by pack-cementation at 1000 °C; (ii) homogenization at 1200 °C to remove concentration gradients and to solutionize the alloyed struts; (iii) aging at 900 °C to form γ' precipitates within the struts. The resulting alloyed foams retain the low relative densities (less than 3%) and open-cell structure with hollow struts of the original pure Ni foams, and they exhibit struts with the γ/γ' structure typical of nickel-base superalloys. The compressive behavior of the superalloy foams, measured at ambient temperature, is compared to model predictions. The creep behavior of the superalloy foams, measured between 680 and 825 °C in the stress range of 0.1–0.3 MPa, is discussed using two models assuming strut compression or strut bending as deformation modes.

Keywords: Chemical vapor deposition; Foams; Nickel alloys; Creep; Precipitation strengthening

1. Introduction

Reticulated ceramic foams have found applications as metal casting filters due to their high permeability and melting point, and as high-temperature insulation in oxidative environment [1–3]. However, ceramic foams are difficult to use for structural, load-bearing applications at elevated temperature, due to their low ductility, toughness and thermal shock resistance. A ductile metallic foam consisting of an oxidation- and creep-resistant alloy could find many load-bearing applications, e.g., as the core of sandwich structures in engines and furnaces, or as high-temperature catalyst substrate, filter, or heat exchanger subjected to thermo-mechanical loads.

Nickel-base superalloys are the preferred alloy system for high-temperature structural applications in air up to ca. 1050 °C. The two most important alloying elements in superalloys are Cr and Al, with Al (sometimes partially replaced with Ti) providing precipitation strengthening by forming coherent γ' Ni_3Al precipitates with the $L1_2$ structure, and with Cr providing solid-solution strengthening of the γ-Ni matrix (and to some extent of the γ' precipitates) [4]. Also, both Cr and Al provide corrosion and oxidation resistance by creating a native, adherent oxide film. Many other transition elements can be further alloyed, mostly to provide solid-solution strengthening of both γ and γ' phases [5]. Thus, a nickel-base superalloy with good creep and oxidation resistance could be the basis for metallic foams with structural applications at temperatures as high as 1050 °C.

To date, very few reports exist on superalloy foams because of the difficulty of processing these high-melting alloys into foams. Queheillalt et al. [6] produced open-cell foams with Inconel 625 composition by electron-beam-directed vapor deposition of the metal onto a polymer foam template. After thermal decomposition of the template, the foams, with relative densities of <3%, were pressureless sintered or transient liquid-phase sintered. No mechanical properties were presented. Bram et al. [7] mixed and pressed pre-alloyed Hastelloy or

* Corresponding author. Tel.: +1-847-491-5933; fax: +1-847-491-7820.
E-mail address: h-choe@northwestern.edu (H. Choe).

1359-6454/$30.00 © 2003 Acta Materialia Inc. Published by Elsevier Ltd. All rights reserved.
doi:10.1016/j.actamat.2003.11.012

Inconel powders with urea powders, which were removed by heating below 200 °C. Subsequent sintering at 1300 °C for 1 h resulted in the partial densification of the Inconel powders while maintaining the hollow spaces (1–1.4 mm in size) previously occupied by the urea powders. The resulting foam, with a relative density of 30%, was not mechanically tested. Finally, Sypeck et al. [8] used hollow Ni 625 spheres (with wt% composition Ni–21Cr–9Mo–4Nb–0.31Al–0.19Ti) created as a by-product of gas atomization. These spheres, with size between 0.36 and 2 mm, were sintered for 24 h at 1300 °C into foams with a relative density of 30–34%. Compressive mechanical properties were reported at ambient temperature, but not at elevated temperature. Recently, Hodge and Dunand [9] demonstrated that NiAl foams, with homogenous Ni–28 to 33 wt% Al composition and the ordered B2 intermetallic structure, could be produced by pack-aluminization of reticulated pure Ni foams. These NiAl foams, with a relative density below 8%, exhibited excellent creep and oxidation resistance [10], but were brittle at ambient temperature, as expected from the very low toughness and ductility of NiAl.

Here, we demonstrate that the pack-aluminization process developed for intermetallic Ni–(28–33) wt% Al foams [9] can be adapted to the production of Ni–(8–9) wt% Al foams, which, after heat-treatment, exhibit the γ/γ' structure typical of superalloys. We also show that Cr can be alloyed to these Ni–Al foams by a similar pack-chromizing technique, resulting in a Ni–Cr–Al foam with superalloy γ/γ' structure. We measure the mechanical properties of these Ni–Al and Ni–Cr–Al foams at both ambient and elevated temperatures, and compare them to predictions of analytical models assuming strut deformation by creep bending [1] or creep compression [10].

2. Experimental procedures

2.1. Processing

Two types of alloyed Ni foam – with composition Ni–(7.8–9.1)Al and Ni–(13.5–16.6)Cr–(5.1–8.9)Al (all compositions hereafter are given in wt%, unless stated otherwise) – were created by pack-cementation of pure Ni foams procured from Porvair (Hendersonville, NC). These pure Ni foams exhibit a reticulated structure consisting of hollow struts with diameter of ca. 224 μm and wall thickness of ca. 84 μm, a cell size of ca. 1.3 mm (20 pores/in. or 20 ppi) and a relative density $\rho^* = 2.2\%$. Figs. 1(a) and (b) show an as-received Ni foam.

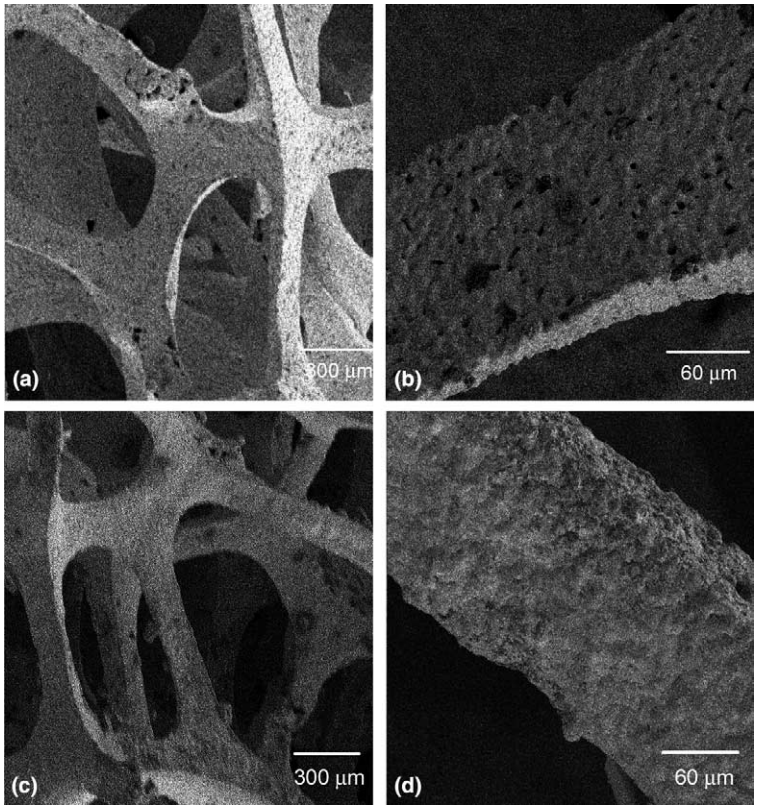

Fig. 1. SEM micrographs showing: (a,b) as-received 20 ppi Ni foams; (c,d) Ni–7.8Al foam aluminized for 15 min at 1000 °C, homogenized for 120 h at 1200 °C, and annealed for 7.5 h at 900 °C.

Aluminization was conducted by pack cementation under argon at 1000 °C, using a high-activity pack composed of 3 wt% NH_4Cl powders as activator, 15 wt% Ni–70 at% Al powders as Al source, and 82 wt% Al_2O_3 powder as filler. After mechanical mixing for ca. 20 min, a total pack mass of 40 g was poured in a high-chromium stainless-steel envelope in which the Ni foam (with typical dimension $10 \times 10 \times 23$ mm and cut by electro-discharge machining) was embedded. The envelope was placed at the water-cooled end of a tube furnace and pushed into the hot zone of the furnace at the process temperature of 1000 °C, where it was left for 10–30 min, depending on the desired composition (in the range of 8–9% Al). Subsequently, the envelope was rapidly pushed to the other water-cooled end of the furnace and allowed to cool to ambient temperature. After removal from the pack, the foam was ultrasonically cleaned to remove any loosely embedded pack materials. Following this first alloying step, the alloyed foam was homogenized at 1200 °C for 120 h under flowing Ar, terminated by quenching in ice-brine. In a third step, aging was performed under flowing Ar at 900 °C for 7.5 h and also terminated by ice-brine quenching.

Some foams were subjected to a chromizing step, which was performed before the aluminizing step, according to the original Cr pack-cementation technique used for coatings of bulk objects [11,12]. The pack composition was 5 wt% NH_4Cl powders as activator, 25 wt% Cr powder, and 70 wt% Al_2O_3 filler powder. The foam and the pack (with mass of 40 g) were contained in the stainless-steel bag, which was placed in the central zone of the unheated furnace under flowing argon, heated for 40–80 min to the process temperature of 1000 °C, and held for varying times before being pushed to the cold end of the furnace to cool. Homogenization was then performed at 1200 °C for 48 h. Foams with a range of compositions in Al (5.1–9.1%) and Cr (13.5–16.6%) were produced by this technique.

Non-porous control samples with a composition (Ni–8%Al) similar to that of the binary Ni–(8–9)Al foams were prepared by arc melting of ca. 30 g of the pure metals into a water-cooled copper mold. The 20-mm diameter button were then homogenized under vacuum at 1200 °C for a minimum of 24 h, drop-quenched into ice-brine, and then sectioned into multiple pieces. Each specimen was aged under argon at 900 ± 5 °C for 7.5 h and then again drop-quenched into ice-brine.

2.2. Mechanical testing

Micro-hardness was measured with a Vickers indenter using a 100-g load on epoxy-mounted specimens which were ground and polished to 0.05 μm colloidal alumina. The compression behavior of the foams was examined at ambient temperature on parallelepiped specimens with $\sim 10 \times 10 \times 23$ mm dimensions, using a servo-hydraulic testing machine with a cross-head speed of 0.1 mm/s. A compression cage ensured parallelism during testing and the strain was determined from the cage platen displacement measured by laser extensometry. The foam compressive strength was determined as the maximum load (divided by the sample cross-section) prior to the onset of substantial crushing.

The creep behavior of the alloyed foam was investigated between 680 and 825 °C in air. The creep tests were performed under constant compressive load, using a compression creep tester (Applied Test Systems, Butler, PA) with a three-zone furnace maintaining temperature within ±2 °C. Pushrod displacement was measured with a linear voltage displacement transducer (Sensotec, Columbus, OH) with an accuracy of ±1 μm. Extreme care was taken to ensure that the upper and lower pushrods were aligned and parallel to each other. The upper pushrod consisted of an alumina tube outfitted with an alumina platen, to minimize the load applied to the specimens by the load train. Premature loading of the sample during heating was prevented by holding the upper alumina tube above the sample without contact until the temperature had equilibrated.

Deformation rates were assessed using a computerized data acquisition system, which calculated the average displacement over a time period long enough to smooth out experimental noise. The strain vs. time data were then differentiated to acquire strain-rate vs. time. This approach gave nearly identical minimum strain rates with an alternative technique where a straight line was fitted to the strain vs. time curve during the secondary creep period.

2.3. Metallography

Specimens were mounted in epoxy and polished down to 0.05 μm colloidal alumina using standard metallographic procedures. The grain size was calculated by the line-intercept method from optical micrographs after etching with a mixture of 10 ml hydrofluoric acid and 100 ml hydrochloric acid. The microstructure was investigated using scanning electron microscopy (SEM), following etching for 10–15 s with a mixture of 50 ml deionized water, 50 ml hydrochloric acid, and 0.5 g potassium metabisulfite. The size and volume fraction of γ' phase were determined by drawing ten random lines of unit length on each SEM micrograph and by conducting intercept measurements [13].

The contiguity $C_{\gamma'}$ of the γ' phase in the two-phase γ–γ' structure (defined by Gurland [14] as the fraction of the total internal surface area of the phase shared with particles of the same phase) was measured following the approach of Fan et al. [15] as:

$$C_{\gamma'} = 2N_L^{\gamma'\gamma'}/(2N_L^{\gamma'\gamma'} + N_L^{\gamma'\gamma}), \quad (1)$$

where $N_L^{\gamma'\gamma'}$ and $N_L^{\gamma'\gamma}$ are the numbers of intercepts of the γ'/γ' and γ'/γ interfaces within a random line of unit length on the examined planes of polish.

3. Results

3.1. Processing

Fig. 2 is a plot of the time-dependence of the Ni foam weight gain upon aluminization and chromization, expressed as average concentration. For Al and Cr content typical of superalloy compositions, the aluminizing and chromizing times are 10–25 and 40–60 min, respectively, well within industrially acceptable times. Fig. 2 illustrates that the foam mass gain rate during chromizing and aluminizing are similar; however, the aluminizing kinetics is markedly slower for Ni–Cr foams containing 16–20% Cr (which were homogenized for 48 h at 1200 °C).

3.2. Macro- and microstructure

Figs. 1(c) and (d) illustrate that, after homogenization and heat-treatment, the Ni–7.8Al foams retain the open-cell, reticulated structure with hollow struts of the original pure Ni foams (Figs. 1(a) and (b)). No macroscopic shape change or distortion was observed in the foam specimens, confirming that mass gain during cementation occurs by deposition of Al or Cr on the strut surface, as previously observed for NiAl foams produced by pack-aluminization [9].

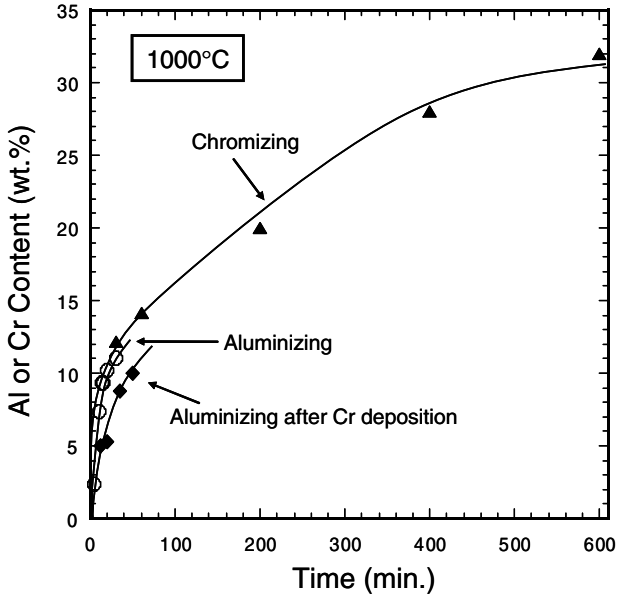

Fig. 2. Time dependence of average composition for Ni foams upon aluminization and/or chromization at 1000 °C.

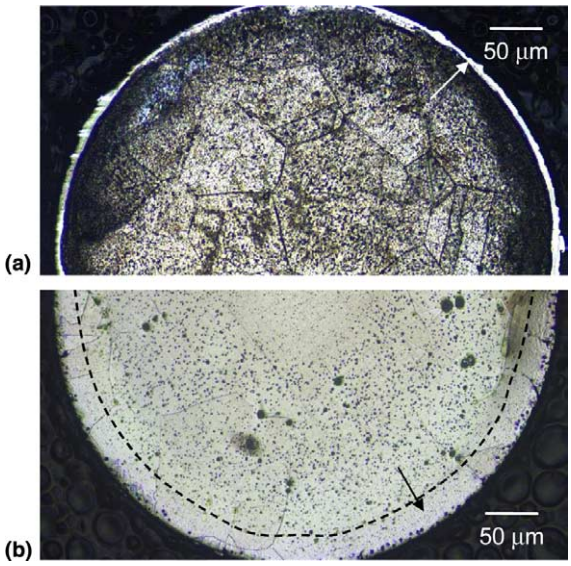

Fig. 3. Optical micrographs showing half of the etched cross-section of 0.5-mm diameter Ni wires (a) chromized for 1 h at 1000 °C, showing a narrow Cr(Ni) layer (arrow); (b) subsequently homogenized for 48 h at 1200 °C, with a broad diffusion Ni(Cr) layer (arrow).

Figs. 3(a) and (b) show optical micrographs of the cross-section of a 0.5-mm diameter nickel wire chromized for 1 h at 1000 °C (Fig. 3(a)) and subsequently homogenized for 48 h at 1200 °C (Fig. 3(b)). Wires were used to visualize the Cr deposit in a geometry much simpler than for the foam struts. Etching was performed by immersion for ca. 40 s into a solution of 10 ml hydrofluoric acid and 100 ml nitric acid. Fig. 3(a) shows that the surface of the Ni wire is coated with a smooth and continuous α-Cr(Ni) layer with a near-uniform thickness of ca. 7 μm. As shown in Fig. 3(b), this thin outer shell disappeared after homogenization by diffusion into the wire. Instead, a wide zone (ca. 40 μm) of alloyed γ-Ni(Cr) is visible as a bright outer ring.

Fig. 4(a) shows the cross-section of a strut for a foam chromized for 2.6 h at 1000 °C (with Ni–19.2Cr composition). As observed for the Ni wire (Fig. 3(a)), a smooth, continuous Cr layer is visible on the whole strut surface, including recessed surfaces. Fig. 4(b) shows the same foam after a 48 h homogenization at 1200 °C. As for the Ni wire (Fig. 3(b)), the Cr layer has dissolved into the struts which show no concentration gradients, and a grain size of 24 ± 5 μm. Finally, an optical micrograph of a strut for a heat-treated, homogenized Ni–17.7Cr–5.3Al foam is shown in Fig. 4(c). As expected, no concentration gradients are visible, and etching reveals a grain size of 43 ± 18 μm. A similar lack of concentration gradients was observed in a Ni–9.1Al foam, with grain size of 47 ± 18 μm.

Representative SEM micrographs of the microstructure for selected, heat-treated Ni–Al and Ni–Cr–Al foams are shown in Figs. 5(a) and (b). Both Ni–Al and Ni–Cr–Al samples exhibit a γ–γ' structure typical of

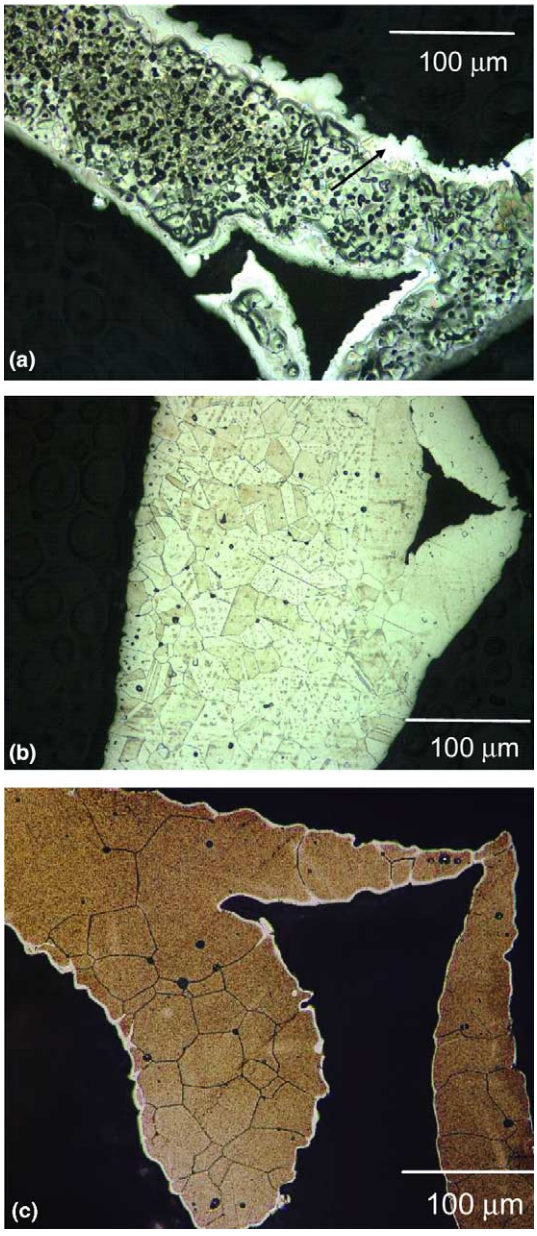

Fig. 4. Optical micrographs for etched struts of Ni foams (a) with average composition Ni–19.2Cr, after chromization at 1000 °C for 2.6 h, showing a narrow Cr(Ni) outer layer (arrow) and a Ni(Cr) interior (with etch pits); (b) same sample subsequently homogenized for 48 h at 1200 °C, showing complete dissolution of the Cr(Ni) layer and etched grain boundaries; (c) homogenized Ni–17.7Cr–5.3Al foam after heat-treatment showing a homogenous structure and etched grain boundaries.

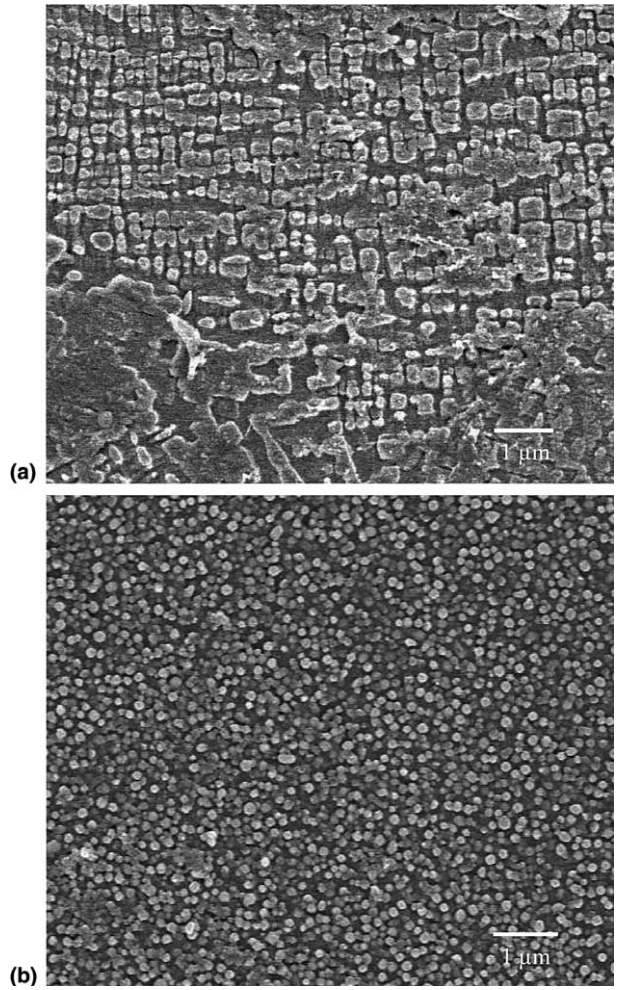

Fig. 5. SEM micrographs of etched foams: (a) Ni–9.1Al, with submicron, cuboidal γ' precipitates in the γ matrix (b) Ni–17.7Cr–5.3Al with finer, spheroidal γ' precipitates in the γ matrix.

Ni-base superalloys [16]. The Ni–9.1Al foam exhibits a 59% volume fraction of γ' precipitates showing a cuboidal or rod-like morphology with interfaces crystallographically oriented within the γ-phase matrix. The Ni–17.7Cr–5.3Al foam contains a slightly lower volume fraction (54 vol%) of mostly spheroidal γ' precipitates which are uniformly dispersed in the γ matrix with no clear crystallographic relationship. The Ni–9.1Al foam has the coarser microstructure, with an average γ' size of 0.36 μm, while the Ni–17.7Cr–5.3Al foam consists of a uniform distribution of finer γ' particles (with average size 0.15 μm). The γ' phase in the Ni–9.1Al foam is semi-continuous in some regions, with an average γ' contiguity $C_{\gamma'} = 0.28$, thrice that in the Ni–17.7Cr–5.3Al ($C_{\gamma'} = 0.094$). The γ' morphological parameters are summarized in Table 1.

3.3. Mechanical properties at ambient temperature

The results of the micro-hardness tests conducted at room temperature are summarized in Table 2. All indentation were made at least 20 μm from the nearest cell strut edge. As the indentation diagonals are all between 15 and 50 μm, the measured hardness is expected to be representative of the multi-phase γ/γ' structure.

Fig. 6 shows the compressive stress–strain curves at ambient temperature for the four foams (Ni, Ni–9Al, Ni–32Cr, and Ni–13.6Cr–8.9Al), with the superalloy

Table 1
γ' particle geometrical characteristics

Alloy (wt%)	γ' volume fraction (%)	Average γ' size (μm)	γ' size standard deviation (μm)	Maximum γ' size (μm)	Minimum γ' size (μm)	Contiguity of γ' $C_{\gamma'}$
Ni–9.1Al	59	0.363	0.205	1.2	0.08	0.280
Ni–17.7Cr–5.3Al	54	0.146	0.057	0.32	0.05	0.094

For γ' with an elongated shape of an aspect ratio greater than unity, the size of the particle is defined as an average of the largest and smallest diameters.

Table 2
Microhardness of struts of heat-treated foams

	Ni ($\rho^* = 2.2\%$)	Ni–32Cr ($\rho^* = 3.5\%$)	Ni–9Al ($\rho^* = 2.6\%$)	Ni–16.6Cr–5.3Al ($\rho^* = 2.9\%$)
Microhardness (HV)	75 ± 3	112 ± 15	571 ± 102	387 ± 92

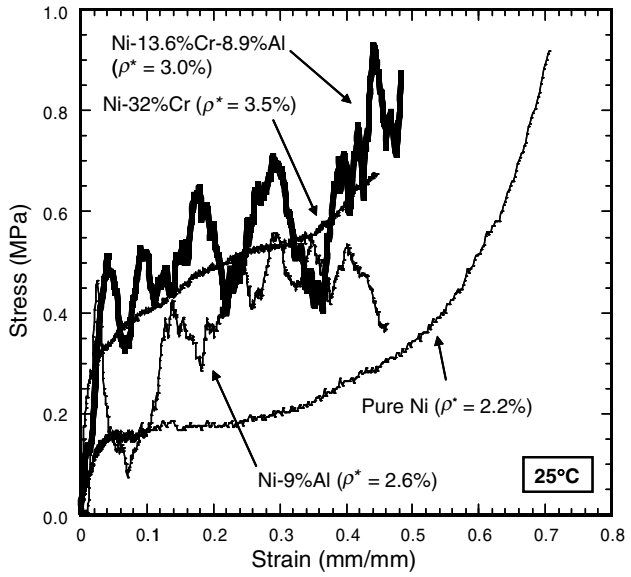

Fig. 6. Room-temperature compressive stress–strain curve of pure Ni, Ni–9Al, Ni–32Cr, and Ni–13.6Cr–8.9Al foams.

foams in the heat-treated condition. The foam stress is given as the applied load divided by the cross-sectional area of the specimen and is thus substantially lower than the stress within the foam struts. The Ni and Ni–Cr curves are smooth, as expected for foams consisting of highly ductile metals; the superalloy foam curves are serrated, probably as a result of localized strut fracture. The superalloy foams kept their integrity up to the maximum strain (ca. 50%) without the macroscopic splitting or spalling typical of fully brittle ceramic foams [17].

3.4. Creep properties

A typical plot of strain vs. time for a Ni–9.1% Al foam during a creep test at 725 °C is shown in Fig. 7(a), resulting in a macroscopically homogeneous deformation, as illustrated in Fig. 7(b). The foam samples

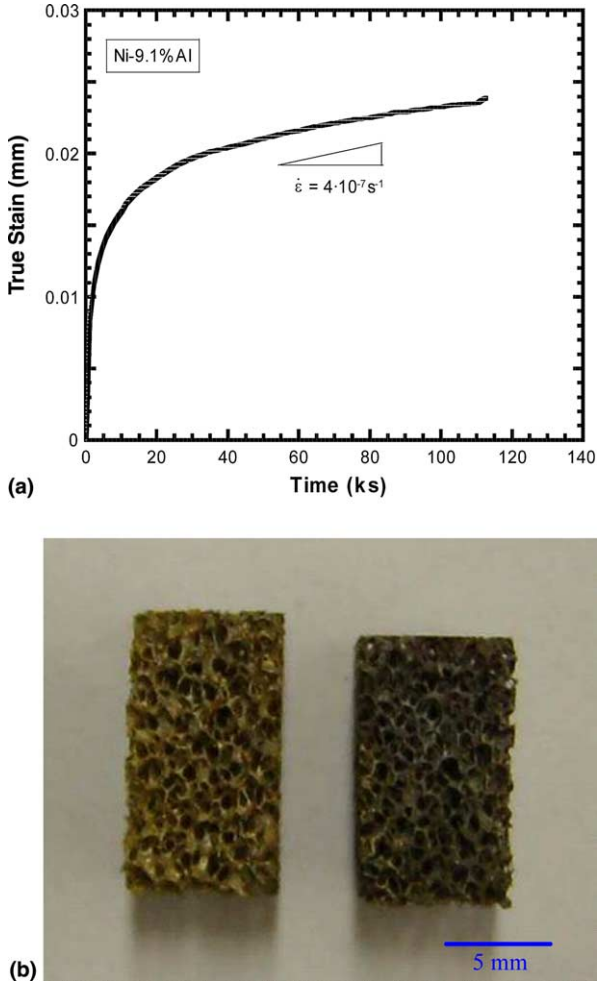

Fig. 7. (a) Typical creep curve for Ni–9.1Al foam ($T = 725$ °C, $\sigma = 0.21$ MPa). (b) Specimens before and after creep test showing a macroscopically uniform deformation.

examined in this study all displayed a primary creep phase with decreasing strain rate, followed by secondary creep regime with a minimum strain rate constant over an extended period of time. Creep in the secondary region was measured for at least 10 h of testing, after

which the sample was subjected to a new load corresponding to a higher stress level. For some specimens tested at higher loads and temperatures, the specimen experienced tertiary-like creep with a rapidly increasing strain rate followed by crushing.

Since the aging temperature of 900 °C was significantly higher than the test temperatures, coarsening during creep was expected to be negligible. This was checked on a Ni–16.6Cr–5.5Al sample, for which neither decrease in room temperature hardness nor loss in creep resistance was observed after creep deformation at 825 °C for ca. 20 h, indicating that no or insignificant coarsening of γ' precipitates occurred during the previous creep test.

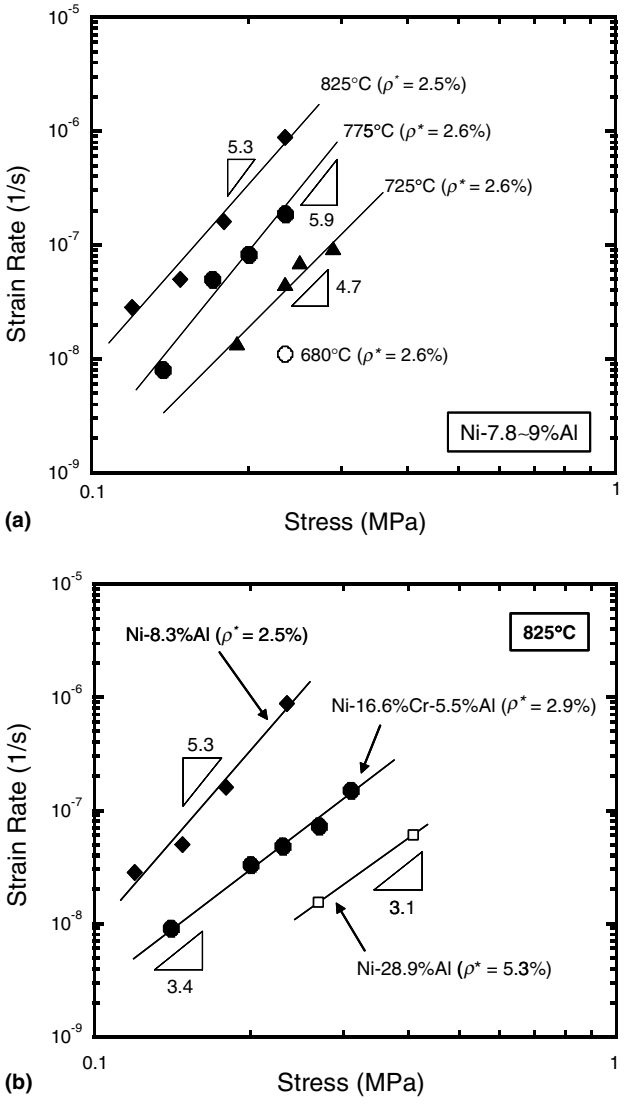

Fig. 8. (a) Secondary strain rate plotted against stress at constant temperatures between 680 and 825 °C for Ni–Al foams ($\rho^* = 2.5$–2.6%). (b) Secondary strain rate for Ni–8.3Al and Ni–16.6Cr–5.5Al foams ($\rho^* = 2.9\%$) plotted against stress at a constant temperature of 825 °C. Data for a Ni–28.9Al intermetallic foam ($\rho^* = 5.3\%$) [10] are also plotted.

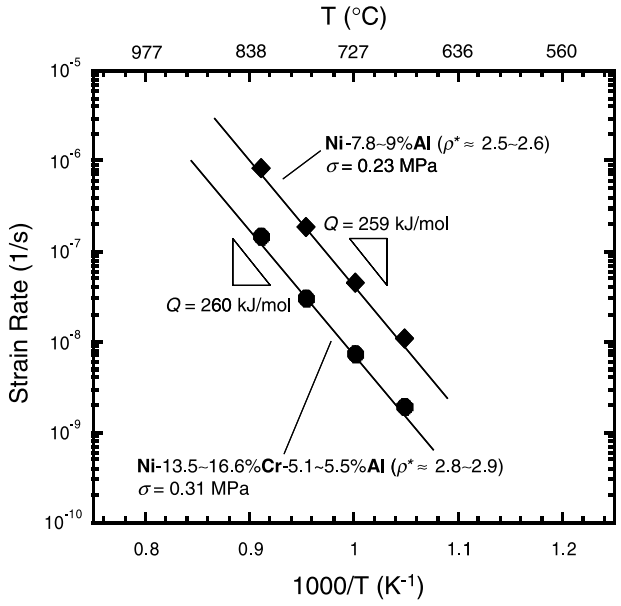

Fig. 9. Secondary creep rate plotted against the inverse of temperature at a constant stress of 0.23 and 0.31 MPa for Ni–Al and Ni–Cr–Al foams, respectively.

The power-law stress exponent n was determined from double-logarithmic plots of secondary strain rate vs. stress. For Ni–Al superalloy foams, as shown in Fig. 8(a), $n = 4.7$, 5.9, and 5.3, for $T = 725$, 775, and 825 °C, respectively. The average value, $n = 5.3$, is within the range observed for power-law dislocation creep of Ni-base superalloy ($n = 3.5$–6 [18,19]). The secondary creep rates for Ni–Cr–Al superalloy foams at 825 °C are compared in Fig. 8(b) with those for the Ni–Al superalloy foams. It is apparent that the creep strain rate for the Ni–Cr–Al foam is ca. one order of magnitude lower than that of the Ni–Al foam. Also, the creep exponent for the Ni–Cr–Al foam ($n = 3.4$) is significantly lower than that for the Ni–Al foam ($n = 5.3$).

Two sets of tests, where the temperature was varied ($T = 680$–825 °C) and the stress was held constant ($\sigma = 0.23$ MPa for the Ni–Al foams and $\sigma = 0.31$ for the Ni–Cr–Al foams), were conducted to determine the creep activation energy, as shown in Fig. 9. Unlike the stress exponent, n, the activation energy for Ni–Al and Ni–Cr–Al foams is the same within experimental error (259 kJ/mol for Ni–Al and 260 kJ/mol for Ni–Cr–Al), close to the value for bulk superalloys ($Q = 285$ kJ/mol) [20] and for pure Ni ($Q = 284$ kJ/mol) [21].

4. Discussion

4.1. Processing

Ammonium chloride was used as an activator for both chromizing and aluminizing, as it was shown to be

more effective than other activators in chromium transport [12]. The present results indicate that bulk chromizing methods developed for objects with low specific areas [12,22,23] can be used successfully for reticulated foams with high specific area, without macroscopic composition gradients between the struts near the specimen core and those near the specimen surface. As illustrated in Fig. 4(a), the chromizing step allows for a very uniform deposition of Cr onto the strut surface, including recessed surfaces. This is important, since uneven deposition would lead to composition gradients within the foams after homogenization.

The long homogenization time used for the cemented foams (5 days at 1200 °C) was based on calculations for diffusion distance of Al and Cr atoms. Using tracer diffusion constants D given in [18,24], a time $t = 120$ h at 1200 °C corresponds to a representative diffusion distance $(6Dt)^{1/2} = 559$ μm for Al and 344 μm for Cr. This time is well in excess of that needed to homogenize the composition along the strut wall thickness (ca. 84 μm) and is sufficient to erase most of the gradients along strut length (ca. 700 μm). Such gradients could occur if the walls thickness of the joints connecting the struts is larger than that of the struts away from the joints in the as-received Ni foams. A complex microstructural analysis, not performed here, would be needed to ascertain whether such wall thickness variations are present in the as-received foams. If the wall thickness is constant, then much shorter annealing times would be possible, e.g., about 7 h at 1200 °C.

The Ni–Cr phase diagram [25] predicts that, at 1000 °C, ca. 7 wt% Ni can be in solution in α-Cr and 41 wt% Cr in γ-Ni. A significant amount of the Cr deposited in Figs. 3(a) and 4(a) has thus diffused in the Ni, leaving only a thin α-Cr(Ni) outer shell, visible as an un-etched ring in Fig. 3(a), since high-Cr coatings are not easily etched by the etchant used here [11]. At 1200 °C, the solubility of Cr in γ-Ni is 46 wt% and of Ni in Cr is 32 wt% [25]; the large outer ring visible in Fig. 3(b) after 48 h at 1200 °C, thus probably consists of alloyed γ-Ni(Cr). As expected from the phase diagram, no intermetallic phases are visible, and the wire consists of a solid solution of Cr in Ni with the Cr concentration increasing toward the surface [12]. The situation for Al deposited onto Ni is much more complex, given the three intermetallic phases present in the Ni–Al system [25]; a complete analysis of diffusion of Al into Ni wires and foam struts is given elsewhere [27].

As expected for a diffusion-controlled mechanism, the kinetics for both aluminization and chromization exhibits a monotonously decreasing time dependence (Fig. 2) [9,26]. However, a simple parabolic behavior is not expected, as the diffusion problem is complicated by the presence of multiple intermetallic phases (for aluminization), moving phase boundaries [9], and non-planar geometry, as modeled in [27] for the case of aluminization. Fig. 2 also shows that mass gain rate during chromizing is somewhat greater that during aluminizing, despite the fact that Cr diffusion is slower than Al diffusion by a factor of 2.5 at 1000 °C [18]. This effect may be due to different rates of metal transport in the gas phase and/or to the much higher solubility of Cr in Ni as compared to Al in Ni (40 vs. 6 wt% at 1000 °C) [25]. The lower aluminizing kinetics for the Ni–Cr foams as compared to pure Ni foams may be due to a diffusion coefficient and/or solubility for Al which is lower in Ni(Cr) than in pure Ni at 1200 °C. Finally, we note that simultaneous deposition of Al and Cr (chrom-aluminizing) is possible [11,22,23], but was not attempted here to maintain a precise control of Al content, which is critical given the relatively narrow Al composition range for useful γ′ volume fractions.

4.2. Microstructure

The grain size after homogenization at 1200 °C is large (ca. 45 ± 21 μm for the Ni–Al and Ni–Cr–Al foams), as compared to the 13 ± 6 μm grain size of the as-received Ni foams probably due to grain growth at the high homologous temperature $T/T_m = 0.85$. In terms of creep resistance, a coarse grain size is desirable to prevent diffusional creep, but a bamboo structure (where a single grain spans the whole wall thickness) must be avoided. The present grain size of 45 μm is near optimal, given the average wall thickness of 84 μm.

The shape and size of the γ′ precipitates is strongly affected by the presence of Cr, as illustrated in Figs. 5(a) and (b): the Ni–9.1Al foam exhibits larger precipitates with cuboidal or rod-like shape with a definite crystallographic orientation with respect to the matrix, while for the Ni–17.7Cr–5.3Al foam, precipitates are smaller and mostly spheroidal, with no clear crystallographic orientation. First, the difference in size can be explained by the slower diffusion in Ni of Cr as compared to Al, which slows down the coarsening the γ′ precipitates, as Cr is present in the precipitates. Second, two possible mechanisms can explain the change of morphology: (i) the Ni–Cr–Al foams exhibit smaller γ′ precipitates than the Ni–Al foams (Table 1) and it is known that small γ′ precipitates are spheroidal, while larger ones become facetted, cuboidal and eventually rod- or plate-like; (ii) Cr reduces the mismatch between the γ and γ′ phases, thus favoring the spheroidal shape [28–30].

In Fig. 5(a), many of the γ′ precipitates in the Ni–Al foams are split into a pair of parallel plates. This splitting phenomenon is known to result from elastic interactions between γ′ particles compensating for the marked increase in surface energy due to the split [31].

4.3. Mechanical properties at ambient temperature

The hardness value for the Ni–32Cr foam is slightly higher than that of the pure Ni foam (112 and 75 HV,

respectively, Table 2), which is in good agreement with results by Owusu-Boahen et al. [32]. The average microhardness values for the Ni–9Al and Ni–16.6Cr–5.3Al foams are however much higher (571 and 387 HV, respectively, Table 2). This confirms that the majority of the strengthening in these alloys originates from the γ' precipitates, not from the solid-solution strengthening of the γ matrix by Cr. Both hardness values are comparable to those of Ni-base superalloy IN 738, ranging from 350 to 460 HV, depending on aging history [4]. The rather large scatter in hardness for Ni–9Al and Ni–16.6Cr–5.3Al (Table 2) is attributed to variations in composition due to variation in strut thickness. Finally, the less continuous ($C_{\gamma'} \sim 0.094$, Table 1) distribution of γ' phase in this Ni–17.7 Cr–5.3Al foam along with its lower Al contents and hence lower volume fraction are probably the prime reasons for its lower hardness as compared to that of the Ni–9.1Al foam.

As illustrated in Fig. 6, the stress–strain behavior of the Ni and Ni–Cr foams is typical of ductile metallic foams: linear elasticity at low stresses, followed by a long collapse plateau, and finally a densification regime where the stress rises steeply. In contrast, both heat-treated superalloy foams exhibit a more brittle behavior, which may be due to the much higher strength of the alloy, as illustrated by the hardness values (Table 2). The significantly higher yield stress of the alloyed foams as compared to the Ni foam is due both to their higher density (following mass gain during the cementation process) and to solid-solution strengthening (for the Ni–Cr foams) or precipitation strengthening from the γ'precipitates (for the superalloy foams). The relative importance of these mechanisms is expressed in a model for the yield stress of open-cell metallic foams (derived by assuming formation of plastic hinges at the strut joints [1]):

$$\sigma_y^* \approx 0.3\sigma_y \rho^{*3/2}, \quad (2)$$

where σ_y is the yield strength of the bulk material and ρ^* is the relative density of the foam. Using reasonable estimations based on literature data for the yield stress of Ni, Ni–32Cr and heat-treated Ni–9Al and Ni–13.6Cr–8.9Al, the foam yield stresses predicted from Eq. (2) are in rough agreement with our experimental values, as shown in Table 3. The agreement is acceptable, given that Eq. (2) predicts within a factor of ca. 2 the yield stress at ambient temperature of aluminum foams with relative densities in the range of 3–40% [33]. Also, the jagged shape of the stress–strain curves for the superalloy foams indicates that large errors are attached to the value of the yield stress (taken as the maximum stress before initiation of collapse).

4.4. Creep properties

As shown in Fig. 8(b), the Ni–16.6Cr–5.5Al foams display creep rates which are ca. 10 times lower than for the Ni–8.3Al foams. This effect may be attributed to three reasons, i.e., increase in relative foam density, solid-solution strengthening by Cr, and improved γ' particle morphology. At constant temperature and stress, the creep rate of open cell foams varies with the relative density ρ^* raised to the power $-(3n+1)/2$ according to the model by Andrews et al. [34], or to the power n according to the model by Hodge and Dunand [10] (both models are discussed in more details in the following section). Taking a value of n for the Ni–Al foams to be 5.3 (as described in the following section) and the experimental values of 2.5% and 2.9% for the relative density of the Ni–Al and Ni–Cr–Al foams, respectively, these models predict a decrease in creep rate by a factor of 2.2–3.5 from the Ni–Cr to Ni–Cr–Al foams based solely on increased density. This is less than the observed factor 10 decrease, implying that one or more other effects are active. First, chromium in solid solution within nickel slows down the creep rate by ca. one order of magnitude for the present level of 17 wt% [21], which is sufficient to explain the observed improvement in Fig. 8(b). Second, the effect of the size, shape, and distribution of the γ' precipitates is difficult to predict. On the one hand, due to their lower Al content, the Ni–16.6Cr–5.5Al foams have a volume fraction of γ' lower than the Ni–8.3Al foams (as reported in Table 1 for slightly different compositions), thus decreasing creep resistance. On the other hand, the Ni–16.6Cr–5.5Al foams exhibit γ' precipitates which are finer in size and more uniformly dispersed in the matrix, both effect increasing creep resistance as compared to the Ni–8.3Al foams.

Table 3
Yield strength of foams at room temperature

	Relative density, ρ^* (%)	Estimated bulk yield strength, σ_y (MPa)	Predicted foam yield stress, σ_y^* [Eq. (2)] (MPa)	Experimental foam yield stress, σ_y^* (MPa)
Ni	2.2	90,150 [18]	0.09–0.15	0.15
Ni–32%Cr[a]	3.5	260 [25]	0.51	0.30
Ni–9Al[b]	2.6	370 [25]	0.41	0.46
Ni–13.6Cr–8.9Al[b]	3.0	550 [25]	0.85	0.52

[a] After homogenizing.
[b] After homogenizing and annealing.

As also shown in Fig. 8(b), the creep rates of Ni–Cr–Al foams creep rates are ca. 10 times higher than for the intermetallic NiAl foams measured in [10]. The first two reasons invoked above, i.e., increased relative density ($\rho^* = 2.9\%$ vs. 5.3%) and changes in material creep resistance (Ni–Cr–Al vs. NiAl), can contribute. Using the creep data for solid NiAl given in [10], the intrinsic creep resistance of NiAl as compared to Ni–Cr–Al, as expressed in terms of inverse strain rate, is similar between 10 and 20 MPa but higher above 25 MPa (i.e., by a factor of 10 at 60 MPa, the upper range of the stress expected in the struts of the foams). We thus again conclude that the better creep resistance of the intermetallic NiAl foams is due to both increased foam density and higher intrinsic creep resistance of the strut material.

4.5. Analytical creep models

Creep of metallic foam has been modeled by Gibson and Ashby [1], who assumed a unit cell where joints consist of two horizontal and one vertical strut (shown schematically in inset of Fig. 10(a)). The vertically applied load is transmitted through the vertical struts (assumed to remain rigid) to the horizontal struts, which deform by creep bending. The foam steady-state creep rate $\dot{\varepsilon}^*$ is then predicted to be

$$\dot{\varepsilon}^* = K\frac{0.6}{(n+2)}\left(\frac{1.7(2n+1)}{n}\right)^n \sigma^{*n}\rho^{*-(3n+1)/2}\exp\left(\frac{-Q}{RT}\right), \tag{3}$$

with the same Dorn constant K, stress exponent n, and activation energy Q as the bulk metal, assumed to deform according to a power-law where the strain rate $\dot{\varepsilon}$ is related to the uniaxial applied stress σ as

$$\dot{\varepsilon} = K\sigma^n \exp\left(\frac{-Q}{RT}\right), \tag{4}$$

where R is the gas constant and T is the temperature. Eq. (3) was developed for non-hollow struts, but the hollow strut geometry does not affect the predictions of the creep-bending model appreciably for the present high ratio of wall thickness to strut diameter [35].

Another model was developed recently by Hodge and Dunand [10], assuming that vertical struts deform by creep compression, while horizontal struts remain rigid, and only prevent buckling of the vertical struts (illustrated in inset of Fig. 10(b)). The foam creep rate $\dot{\varepsilon}^*$ is then predicted to be

$$\dot{\varepsilon}^* = K\left(\frac{\rho^*}{3}\right)^{-n}\sigma^{*n}\exp\left(\frac{-Q}{RT}\right). \tag{5}$$

As illustrated in Figs. 10(a) and (b), for the Ni–Al foams a linear regression analysis of Eqs. (3) and (5) by the least-squares method gives almost the same values for both n and Q, which are the two unknowns in those equations: $n = 5.4$ and $Q = 248$ kJ/mol for the creep bending model; $n = 5.4$ and $Q = 252$ kJ/mol for the creep compression model. Eq. (5) exhibits a slightly better fit than Eq. (3), with a somewhat lower residual sum of difference squared (0.67 vs. 0.80). A similar situation was observed when comparing both models to creep data of NiAl foams [10].

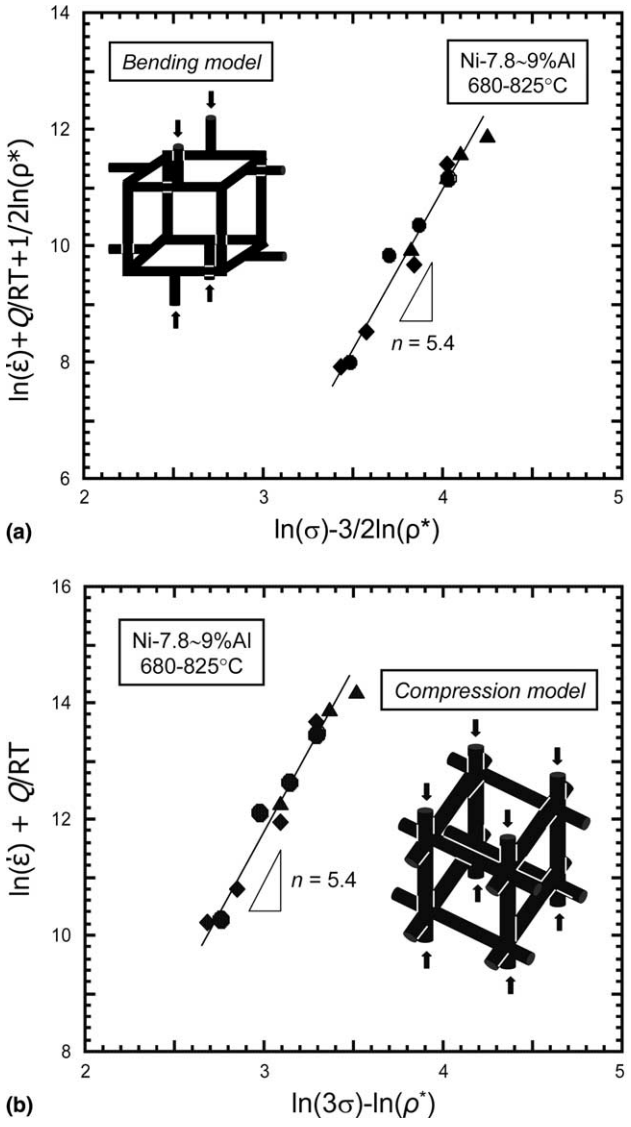

Fig. 10. Compressive creep data for Ni–Al foams ($\rho^* = 2.5$–2.6%) for the temperature range of 680 and 825 °C plotted according to (a) Eq. (3) and (b) Eq. (5). Unit cells are shown as insets.

However, both bending and compression models give widely different values for the adjustable parameter, K. To differentiate between the models, it is thus necessary to measure independently all three creep parameters (K, Q, and n) on non-porous Ni–Al superalloy samples. To this end, a series of creep experiments was performed on samples of arc-melted, solid Ni–8 wt% Al alloy with the same heat-treatment as the foams (homogenization at 1200 °C for 48 h and annealing at 900 ° for 7.5 h). Fig. 11(a) plots the secondary creep strain rate of these

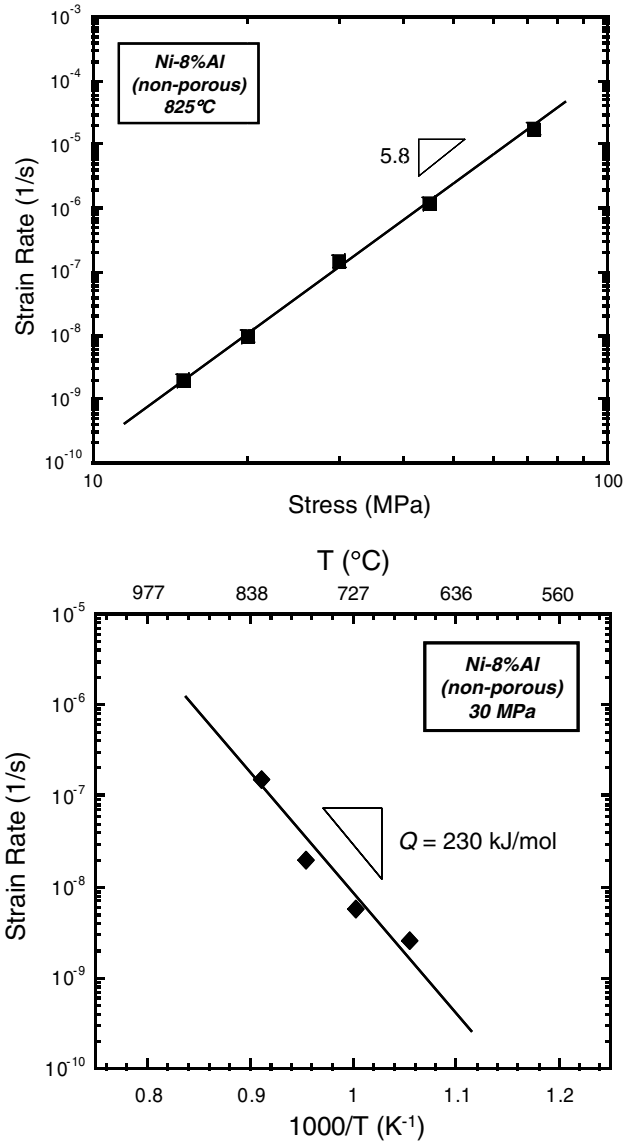

Fig. 11. (a) Secondary compressive strain rate plotted against stress at a constant temperature $T = 825$ °C for arc-melted, heat-treated Ni–8%Al samples, showing a stress exponent $n = 5.8$; (b) Secondary strain rate plotted against the inverse of temperature at a constant stress of 30 MPa for arc-melted, heat-treated Ni–8%Al samples, showing an activation energy $Q = 230$ kJ/mol.

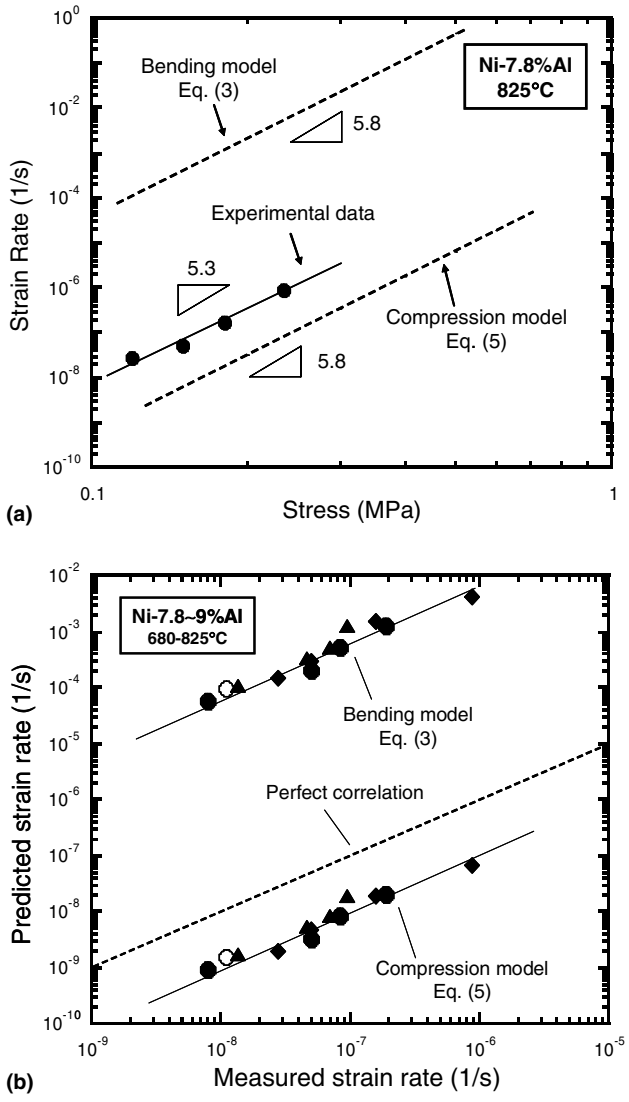

Fig. 12. (a) Comparison between experimental creep data for Ni–7.8Al foams ($\rho^* = 2.5\%$) at 825 °C and predictions of analytical models assuming creep bending of struts [Eq. (3)] or creep compression of struts [Eq. (5)]. (b) Comparison between experimentally measured creep rates for Ni–(7.8–9%)Al foams with $\rho^* = 2.5$–2.6% between 680 and 825 °C plotted on the x-axis and creep rates predicted from creep bending [Eq. (3)] and creep compression [Eq. (5)] models on the y-axis. Dotted line represents a perfect correlation and solid lines best-fit regressions.

solid Ni–8%Al samples as a function of the stress at a constant temperature of 825 °C, from which a stress exponent $n = 5.8$ is determined. Fig. 11(b) plots the secondary creep rate of the solid samples as a function of inverse temperature at a constant stress of 30 MPa, resulting in an activation energy $Q = 230$ kJ/mol. A double regression analysis of the data for the solid samples then provides the Dorn constant as $K = 4.2 \times 10^{-5}$ MPa$^{-5.8}$ s^{-1}. Using these creep constants as input into Eqs. (3) and (5), the models can be compared to data for the Ni–Al foams without any adjustable parameter; this is done in Fig. 12(a), where the strain rate is plotted as a function of stress at 825 °C for the Ni–Al foams. The creep strain rates as predicted by the models differ by ca. five orders of magnitude, with the experimental values falling between the two predictions. The creep compression model [Eq. (5)] underestimates the experimental creep rates by ca. one order of magnitude, while the creep bending model [Eq. (3)] overestimates the experimental data by ca. four orders of magnitude. A very large overprediction of experimental data by the creep bending model has also been observed in open cell aluminum foams [34] and NiAl intermetallic foams [10].

Fig. 12(b) shows a comparison between the predicted strain rates for both models and the experimentally measured values at all temperatures (680–825 °C) and Ni–Al foam densities ($\rho^* = 2.5$–2.6%). As expected, the experimental creep data fall between the two models, which represent extreme cases: the bending model corresponds to a particularly weak geometry, where three struts converge into each cell joint, while the creep compression model is for a strong geometry, where six struts converge into each joint. A previous study for NiAl foams produced by pack cementation [10] found the experimental data within a factor of 2 of the compression creep predictions. In the present Ni–Al superalloy foams, the discrepancy is wider, ca. a factor of 10. A possible reason is that the current superalloy foams are very sensitive to small composition variations which affect strongly the volume fraction of γ' precipitates. Composition variations are expected due to variation in Ni foam thickness, especially at the strut joints, where excess Ni will lead to lower local Al concentration (which could not be completely erased by the long homogenization times), and thus lower γ' fraction and creep resistance. On the other hand, the creep properties of NiAl are relatively insensitive to composition within the wide range of Al-composition for the B2 intermetallic [10]. As previously noted in that study [10], it thus seems that the connectivity of struts at the joints should determine which analytical model is better suited for a given metallic foam: the strut creep-bending model [Eq. (3)] if few struts converge into joints, the strut creep-compression model [Eq. (5)], if the joints consist of many more struts.

5. Conclusions

- The pack-aluminization process previously developed to synthesize intermetallic NiAl foams from pure Ni foams [9] was adapted to the production of Ni foams with 8–9 wt% Al, within the γ/γ' two-phase region. Chromium was added to these Ni–Al foams by a similar packchromizing technique, resulting in an Ni foam with 14–18 wt% Cr and 5–9 wt% Al. After heat-treatment, both Ni–Al and Ni–Cr–Al foams exhibited submicron γ' precipitates in a γ matrix, typical of Ni-base superalloys, and relative densities $\rho^* = 2.5$–3.0%.
- At room-temperature, the alloyed foams exhibit a compressive yield strength (ca. 0.50 MPa), about thrice that of the pure Ni foam (0.15 MPa), as a result of increased foam density and higher alloy strength.
- Ni–Al and Ni–Cr–Al foams exhibit stress exponents and activation energies similar to those of bulk Ni-base superalloys. Cr additions increased the creep resistance as a result of increased foam density, solid-solution hardening of the γ matrix, and modification of γ' precipitate morphology.
- Inserting creep parameters independently determined on a Ni–Al superalloy of the same composition into two analytical creep foam models (assuming struts deforming by creep bending and creep compression, respectively) provides predictions which bracket the experimental creep data for the Ni–Al superalloy foams. These foams are closer to the model assuming creep compression than to the model assuming creep bending, as observed previously for intermetallic NiAl foams.

Acknowledgements

This research was supported by NASA through Grant NCC3-870. The authors thank Dr. M.V. Nathal (NASA Glenn Research Center) and Dr. A.M. Hodge (Lawrence Livermore National Laboratory) for useful discussions and Mr. J. Marvin (Northwestern University) for preliminary experiments.

References

[1] Gibson LJ, Ashby MF. Cellular solids: structure and properties. Oxford, UK: Pergamon Press; 1988.
[2] Huang JS, Gibson LJ. Acta Metall Mater 1991;39(7):1627.
[3] Brezny R, Green DJ, Dam CQ. J Am Ceram Soc 1989;72(6):885.
[4] Steven RA, Flewitt PE. J Mater Sci Engrg 1979;37:237.
[5] Gessinger GH. Powder metallurgy of superalloys. London, UK: Butterworth & Co.; 1984.
[6] Queheillalt DT, Hass DD, Sypeck DJ, Wadley NG. J Mater Res 2001;16(4):1028.
[7] Bram M, Stiller C, Buchkremer HP, Stöver D, Baur H. Adv Engrg Mater 2000;2(4):196.
[8] Sypeck DJ, Parrish PA, Hayden HNG. In: Schwartz DS, Shih DS, Wadley HNG, Evans AG, editors. Porous and cellular materials for structural applications. Warrendale, PA: MRS; 1998. p. 205.
[9] Hodge AM, Dunand DC. Intermetallics 2001;9:581.
[10] Hodge AM, Dunand DC. Metall Mater Trans 2003;34A:2353.
[11] Geib FD, Rapp RA. Oxid Metals 1993;40:213.
[12] Godlewska E, Godlewski K. Oxid Metals 1984;22:117.
[13] Annual book of ASTM standards. Philadelphia, PA: ASTM; 2000. p. 3.01.
[14] Gurland J. Trans TMS-AIME 1958;212:452.
[15] Fan Z, Miodownik AP, Tsakiropoulos P. Mater Sci Technol 1993;9:1094.
[16] Durand-Charre M. The microstructure of superalloys. Amsterdam, The Netherlands: Gordon & Breach; 1997.
[17] Dam CQ, Brezny R, Green DJ. J Mater Res 1990;5(1):163.
[18] Smithells CJ. Smithells metals reference book. Boston, MA: Oxford; 1992.
[19] McLean M. Acta Metall 1985;33(4):545.
[20] Ignat M, Dupeux M, Rouault-Rogez H. In: Kettunen PO, Leppistö TK, Lehtonen ME, editors. International Conference on the Strength of Metals and Alloys, vol. 2. Finlnd: Tampere; 1988. p. 899.
[21] Frost HJ, Ashby MF. Deformation-mechanism maps: the plasticity and creep of metals and ceramics. New York, NY: Pergamon Press; 1982.
[22] Heo NH, Kim MT, Shin JH, Kim CY. Surf Coat Tech 2000;124:39.

[23] Park HH, Lee KT, Shin HS. Oxid Metals 1998;50:377.
[24] Gust W, Hintz MB, Lodding A, Odelius H, Predel B. Phys Stat Sol 1981;64:187.
[25] ASM-handbook. Heat treatment, structure and properties of nonferrous alloys. Metals Park, OH: ASM; 1984.
[26] Zhou C, Xu H, Gong S, Kim KY. Mater Sci Engrg 2003;A341:169.
[27] Dunand DC, Hodge AM, Schuh C. Mater Sci Technol 2002;18:326.
[28] Maheshwari A, Ardell AJ. Acta Metall Mater 1992;40(10):2661.
[29] Phillips VA. Acta Metall 1966;14:1533.
[30] Lund AC, Voorhees PW. Acta Mater 2002;50:2085.
[31] Doi M, Miyazaki T, Wakatsuki T. Mater Sci Engrg 1984;67:247.
[32] Owusu-Boahen K, Bamberger M, Dirnfeld SF, Prinz B, Klodt J. Mater Sci Technol 1996;12:290.
[33] Andrews EW, Huang J-S, Gibson LJ. Acta Mater 1999;47:2927.
[34] Andrews EW, Gibson LJ, Ashby MF. Acta Mater 1999;47:2853.
[35] Goretta KC, Brezny R, Dam CQ, Green DJ, De Arellano-Lopez AR, Dominguez-Rodriguez A. Mater Sci Engrg 1990;124A:151.